*Journal of Applied Fluid Mechanics*, Vol. 15, No. 4, pp. 1255-1268, 2022.
Available online at www.jafmonline.net, ISSN 1735-3572, EISSN 1735-3645.
https://doi.org/10.47176/jafm.15.04.1026

# Influence of a Wavy Blade-End Applied in an Axial Compressor Cascade on the Secondary Flow of the Passage

S. Ma†, F. Li, L. Gui, D. Chen and T. Duan

*College of Flight Technology, Civil Aviation Flight University of China, Guanghan, Nanchang Road, 618307, China*

†*Corresponding Author Email: shannirvana@cafuc.edu.cn*

(Received December 15, 2021; accepted February 26, 2022)

## ABSTRACT

To improve the compressor performances at variable conditions, in this research, we used numerical simulation software to analyze and discuss the effects of three kinks of a wavy blade-end on an axial compressor cascade. One of the wavy blade-ends was a traditional structure with a wavy leading edge and a trailing edge (WBE_P). The other two wavy blades were new structures with a straight trailing edge and a wavy leading edge (WBE_R, WBE_S). The difference between WBE_R and WBE_S was that the blade profile used to form the wavy blade was different. For WBE_R, we obtained the wavy leading edge by rotating the element at different heights, and the trailing edge was the center of a circle. For WBE_S, we obtained the wavy leading edge by using a new element with a different camber angle. Because of the new geometry involving some discussions of a variety of parameters, we further discussed the geometric parameters and structure to guide the design and optimization of the blade. We drew some conclusions at the stable condition (6° incidence). For the first case (WBE_P), when the wavelength of the wavy blade-end was increased to 0.3 times the blade height, the total pressure loss was enhanced. When the wavelength was 0.2 times the blade height, the amplitude was 0.06 times the pitch, the minimum area of blocked range ($A_b$) and the total pressure loss coefficient $\zeta$ could be obtained, and the $\zeta$ and $A_b$ were decreased by 5.49%, and 12.72% compared with the baseline. Furthermore, to weaken the influence of changed blade profile on the exit airflow angle, we proposed WBE_P and WBE_R with new structures. We further improved the flow-field characteristics of WBE_P by WBE_R, and the $\zeta$ and $A_b$ decreased by 5.84% and 13.79% compared with the baseline. Additionally, the stall point was delayed from 7.5° to 7.7° incidence. Therefore, the wavy blade-end applied in the leading edge had a greater contribution to improving the flow characteristic, and the straight trailing edge was beneficial to maintaining the exit flow angle. WBE_S with a smoother blade surface did not show an advantage compared with WBE_R. WBE_R with a wavy blade-end leading edge and a straight trailing edge showed an advantage in improving the cascade performance, which was suitable for use in the stator from the last stage of a high-load axial compressor.

**Keywords**: Wavy blade-end; Corner separation; Axial compressor cascade; Secondary flow; Flow control.

## NOMENCLATURE

| | |
|---|---|
| $A$ | amplitude of wavy blade-end |
| $A_b$ | rea of blocked range |
| $AR$ | aspect ratio |
| $A_{in}$ | area of inlet boundary |
| $C$ | chord length |
| $Ca$ | axial chord length |
| $Cp$ | static pressure coefficient |
| CV | corner vortex |
| $D_m$ | diffusion parameter |
| DF | diffusion factor |
| $D$ | corner vortex matrix consisting of the database of $H/A$ |
| $H$ | height of wavy blade-end |
| $h$ | height of cascade |
| $i$ | incidence |
| LE | leading edge |
| PS | pressure surface |
| PV | passage vortex |
| $Pt$ | total pressure |
| $P$ | static pressure |
| SS | suction surface |
| SST | shear stress transport |
| SST$\gamma$-$\theta$ | shear stress transport with $\gamma$-$\theta$ transition model |
| TE | trailing edge |
| $t$ | pitch |
| $v_m$ | velocity component of the local main flow |

| | |
|---|---|
| $Z_N$ | non-dimensional Z axis |
| $\alpha_1$ | inlet flow angle of cascade |
| $\alpha_2$ | outlet flow angle of cascade |
| $\beta$ | flow angle |
| $\beta_{1k}$ | inlet metal angle of cascade |
| $\beta_{2k}$ | outlet metal angle of cascade |
| $\gamma$ | stagger angle |
| $\zeta$ | total pressure loss coefficient |
| $\rho$ | density |
| $\tau$ | solidity |
| $\varphi$ | cascade's profile turning angle |

## 1. INTRODUCTION

In recent years, the high-load axial compressor has been widely developed (Xiangjun *et al.* 2014; Pope *et al.* 2021; Ma *et al.* 2019), and serious three-dimensional (3D) corner separation has been found near the end-wall of the last-stage stator. This corner separation is formed mainly as a result of the development of the end-wall boundary layer, which leads to flow loss and a deteriorated flow field (Denton 1993). Many scholars have attempted to improve compressor performance according to passive flow control methods (Hergt and Siller 2015; Payyappalli and Pradeep 2018; Sun *et al.* 2021; Subhra *et al.* 2021) that can reduce the flow loss and extend the stability margin.

The pitchwise movement of the end-wall boundary layer is the main reason for the deterioration of the flow field (Sun *et al.* 2020). Therefore, many flow control schemes that change the boundary layer distribution have been proposed, such as compound lean scheme (Benini and Biollo 2007; Zhihui Li *et al.* 2017), end-wall profile scheme (Kiran and Anish 2017; Hartland *et al.* 2000), and blended blade scheme (Jiabin *et al.* 2018). The boundary layer is redistributed with these methods, and the flow-field characteristics of a compressor are significantly improved. The compound leaned blade was used in an axial compressor cascade by Ding *et al.* (2018), and he pointed out that the leaned blade redistributed the radial pressure near the blade surface, which improved the distribution of the boundary layer. Not only the compressor but also the compound leaned blade introduced in the compressor, as a positive leaned technology, was used in the stator blade of a four-stage compressor by Fischer *et al*. (2004). The total pressure ratio of the compressor was enhanced and the isentropic efficiency was improved (Fischer *et al.* 2004). Furthermore, the compound leaned blade has been used in a real compressor environment. For the design condition, the efficiency can be enhanced by 2%, and the stability margin can be widened by nearly 5% (Wellborn and Delaney 2001).

Wavy blades have been widely studied, and this type of blade can effectively control secondary flow with the wavy surface. A numerical study was carried out by Bearman and Owen (1998). Their results showed that the drag force of a rectangular-section body was reduced by the wavy modification. Furthermore, numerical investigations of the effect of the wavy modification on the flow surrounding a cylinder have been discussed by Lin *et al*. (2013). The reduction of the maximum drag reached 18% when a wavy cylinder with a sinusoidal diameter along the span was used. The stable operating range also can be extended by the application of wavy airfoils based on the numerical studies of Lin *et al.* (2013). The flow separation is mitigated by the wavy airfoil, which delays the occurrence of the stall, and the airfoil aerodynamic performance of the post-stall is improved.

Considering the importance of improving flow characteristics near the end-wall for the cascade performance, a kind of wavy blade near the end-wall was applied in a high-load compressor cascade (Wang *et al.* 2018), which was designed at the blade-end similar to a positive lean profile. The study found that a concave profile used in the blade near the end-wall was beneficial for suppressing the radial pressure gradient and weakening the secondary flow, thus reducing the flow separation. Therefore, the effects of the geometric parameters and structure on the cascade performance should be discussed further. In this research, we applied a one-period sinusoidal curve in a high-load cascade near the end-wall and the named wavy blade-end. We examined the dimensionless wavelength and the amplitude based on the flow characteristics. The objectives of the application of wavy blade-ends are as follows:

1. We proposed three kinds of wavy blade-ends with different profiles and explored and compared their aerodynamic performance.
2. We determined relationship between the dimensionless wavelength, amplitude, and the cascade performance and optimized the structure of the wavy blade-end.
3. We obtained the optimum geometric parameters of the wavy blade-end and discussed the profile characteristics.

## 2. GEOMETRIC PARAMETERS OF CASCADE

The compressor cascade was obtained from Zhang (2010), and the cascade with a high-load profile was selected as the research object to analyze the flow characteristics of the blade passage. The following discussion of the wavy blade-end performance is based on this cascade. The experimental measurement of the baseline was carried out by Zhang (2010). Detailed descriptions of the experiments are presented in the following sections.

The generation of the 3D cascade used a high-load profile, which was from the last stage of a high-pressure compressor. The solidity of the cascade was 2.14. The geometry of the cascade is shown in Fig. 1, and parameters are given in Table 1.

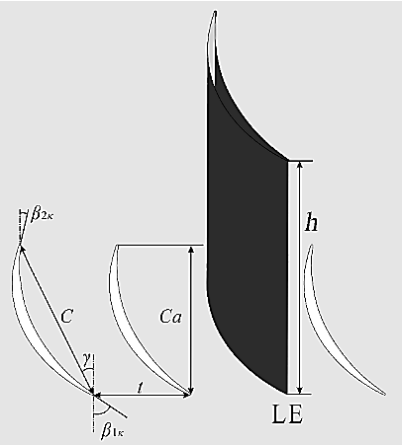


**Fig. 1. Schematic of cascade.**

**Table 1. Geometric and aerodynamic parameters of baseline**

| Parameters | Values |
|---|---|
| Pitch (*t*) (mm) | 53.4 |
| Axial chord length (*Ca*) (mm) | 107 |
| Chord length (*C*) (mm) | 114.3 |
| Full span (mm) | 200 |
| Stagger angle ($\gamma$) (°) | 20.5 |
| Diffusion factor (DF) | 0.5 |

## 3. NUMERICAL SIMULATION METHOD AND VALIDATION

### 3.1 Numerical Model

Considering the periodicity of the cascade, we selected a single passage with a full span as the real 3D computational domain. The mesh and the main boundary conditions are shown in Fig. 2. Hexahedral grids were obtained to generate the computational domain, and two passages are shown for clarity.

The length of the inlet passage was 1.2 times the axial chord length *Ca* to obtain a uniform inflow. The outlet boundary was established as two times the axial chord length *Ca*. The length could guarantee the weakening interference of the exit airflow on the measurement plane. Based on an experiment from Zhang (2010), the measurement plane for obtaining the velocity, pressure, and other parameters was located at a position 0.4 times the axial chord length *Ca* downstream of the TE (leading edge of the blade). In Fig. 2, the walls are covered by the contour of $Y^+$. As shown from the contour, the maximum value of $Y^+$ <1.

The mesh was generated by AutoGrid5 commercial software, and the distribution of grids near the walls is shown in Fig. 3. In the four partially enlarged views, we selected an O-type mesh to surround the blade, which guaranteed the mesh orthogonality, and the mesh refinement was performed near the walls. We adopted H-type meshes to generate the inlet passage and the outlet passage.

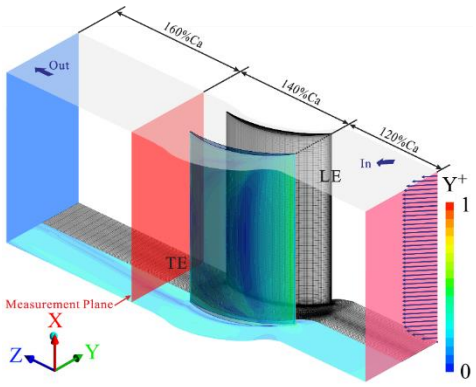


**Fig. 2. Computational domain.**

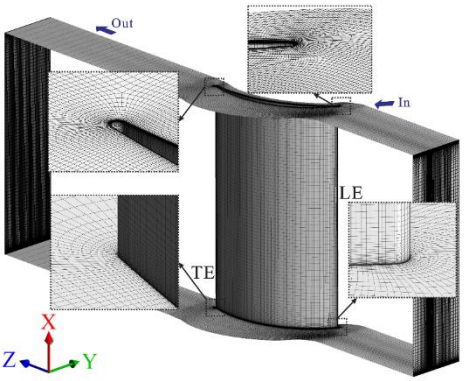


**Fig. 3. Distribution of grids near walls.**

The inflow from the wind tunnel was provided by a radial blower driven by a 45 HP DC motor. The blower could provide a maximum flow of 5 kg/s, and the total pressure rise was 1200 Pa. As shown in Fig. 2, the inlet velocity profile could be found at the inlet section, and the distribution along the spanwise direction was obtained with the experiments. The thickness of the inlet boundary layer on the inlet section was 0.125 times the full span. The average temperature measured experimentally was given on the inlet boundary. The atmospheric pressure was set on the outlet boundary.

In the experiment, we measured the turbulence intensity and the turbulence length scale of the inlet boundary condition mainly by a 55P15 boundary layer probe, as shown in Fig. 4. The L-shaped seven-hole probe (Fig. 5) was arranged on the measurement plane. Then we obtained the pressure, velocity, and other parameters.

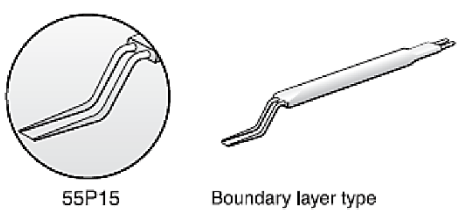


**Fig. 4. Boundary layer probe (Zhang 2010).**

**Fig. 5. L-shaped seven-hole probe (Zhang 2010).**

### 3.2 Turbulence Model

The different closed empirical N-S equations created significant differences in the numerical simulation results. Therefore, it was most important to choose an appropriate turbulence model. We applied the numerical simulation of the 3D cascade using the commercial solver ANSYS CFX, and the advection scheme and turbulence model were set to a high-resolution scheme. The number of grid nodes was 5 million for the verification because the mesh met the requirement of grid independence.

We obtained oil-flow visualizations of the design condition to verify the turbulence model and discuss the flow characteristics. A previous experiment was carried out by Zhang (2010). Figure 6 shows the experimental results for the design condition. Because the cascade was a radially symmetrical structure, we discussed the experimental and numerical results with half-spans.

Figure 7 shows the comparison of numerical simulation results for the SST and SST $\gamma$-$\theta$. Figure 7a shows that the radial separation bubble could not be predicted by the turbulence model SST. However, the position and the axial range of the radial separation bubble were accurately predicted by the SST $\gamma$-$\theta$, and the range of the corner separation was also well captured, as shown in Fig. 7b. Moreover, as shown in Fig. 7c, the separation line SL outlined a corner separation region, the positions of the main nodes $N_1$ and $N_2$ were well estimated, and the range of the separation region was predicted. Only the thickness was underestimated.

Figure 8 shows some limiting streamlines of other turbulent models. An obvious radial separation bubble could be found in the experimental result, but this could not be captured by $k$-$\omega$ and $k$-$\varepsilon$ because these turbulence models did not include transition models. The separation bubble was captured by BSL $\gamma$-$\theta$, but the position was relatively backward-predicted.

To further verify the accuracy of the turbulence model with the transition model, we selected two kinds of inlet velocity distributions with 0.125 span and 0.225 span boundary layers. The comparisons between the numerical and experimental results are shown in Fig. 9. The pitch-average total pressure loss

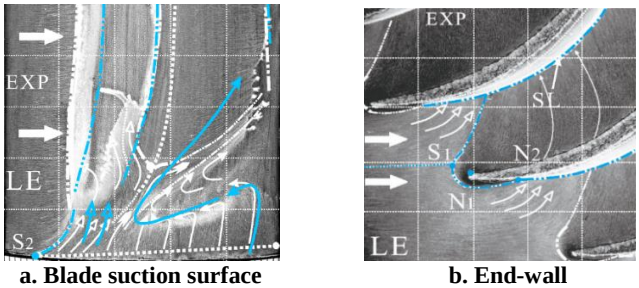


**a. Blade suction surface** **b. End-wall**

**Fig. 6. Oil flow visualizations (Zhang 2010).**

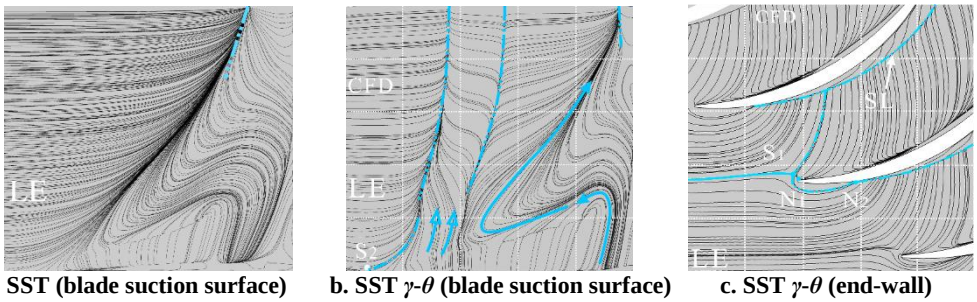


**a. SST (blade suction surface)** **b. SST $\gamma$-$\theta$ (blade suction surface)** **c. SST $\gamma$-$\theta$ (end-wall)**

**Fig. 7. Comparison of SST and SST $\gamma$-$\theta$ .**

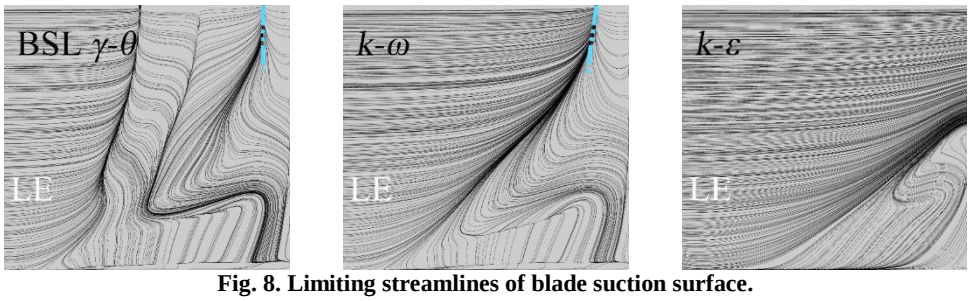


**Fig. 8. Limiting streamlines of blade suction surface.**

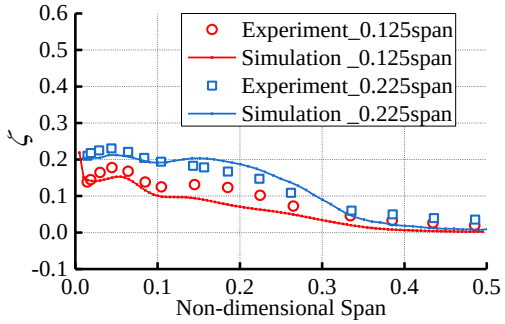


**Fig. 9. Pitchwise averaged $\zeta$ along the spanwise direction.**

coefficient at 40%*Ca* downstream of TE was extracted, and the simulations showed good agreement with the experiment along the full span. In particular, the values near the end-wall were well matched within the 0–10% span, which explained the fact that the numeral calculations should embody the flow behaviors well near the hub to a great extent. Therefore, the turbulence model SST $\gamma$-$\theta$ was appropriate.

The total pressure loss coefficient $\zeta$ was one of the most commonly used parameters to evaluate cascade/stator performance. The formula is given as follows:

$$\zeta(x,y,z)=\frac{Pt_{in}-Pt(x,y,z)}{Pt_{in}-P_{in}} \quad (1)$$

Figure 10 shows the velocity vectors and $\zeta$ at the measurement plane. The left side of the figure shows the experimental result and the right side shows the numerical result. We used this comparison to verify whether SST $\gamma$-$\theta$ could capture the flow-field characteristics well. The black arrows indicate the velocity vectors, and the red solid lines represent the contour lines of the $\zeta$. The distribution of velocity vectors could be well predicted, and the location of the passage vortex (PV) was reproduced accurately. Only the range was underestimated. Additionally, the high-loss region (where the value of the $\zeta$ was bigger than 5.2) was well captured by the simulation method. Only the range along the pitchwise direction was underestimated. Above all, the turbulence model SST $\gamma$-$\theta$ was suitable in this study.

### 3.3 Grid Independence

To save computing resources, we discussed the independence of the grid. We adopted the computational domain with six sets of grids, and the number of grid nodes was from 1.2 million to 5.8 million. The design condition with -1° incidence was selected to analyze the sensitivity of the grid number.

To review the influence of the grid number on the cascade, Fig. 11 provides the mass-flow average $\zeta$ at the different axial positions, and $Z_N$ expresses the dimensionless Z-axis. According to the partially enlarged views, with the increase of grid nodes from 1.2 million to 5.0 million, the $\zeta$ decreased gradually. When the grid nodes were bigger than 5.0 million (such as 5.8 million), the value of the $\zeta$ was the same as that for 5.0 million. Therefore, we selected the mesh with 5 million grid nodes for further research.

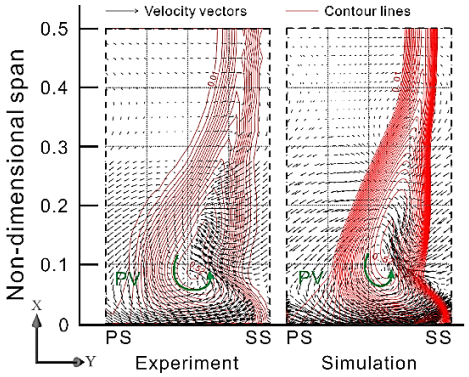


**Fig. 10. Velocity vectors and contour lines of $\zeta$ at the experimental measurement plane.**

## 4. DESIGN OF WAVY BLADE-END

In the formation of 3D compressor blades, the compound lean blade has been extensively studied, such as in the studies carried out by Benini and Biollo (2007). The thickness of the boundary layer near the

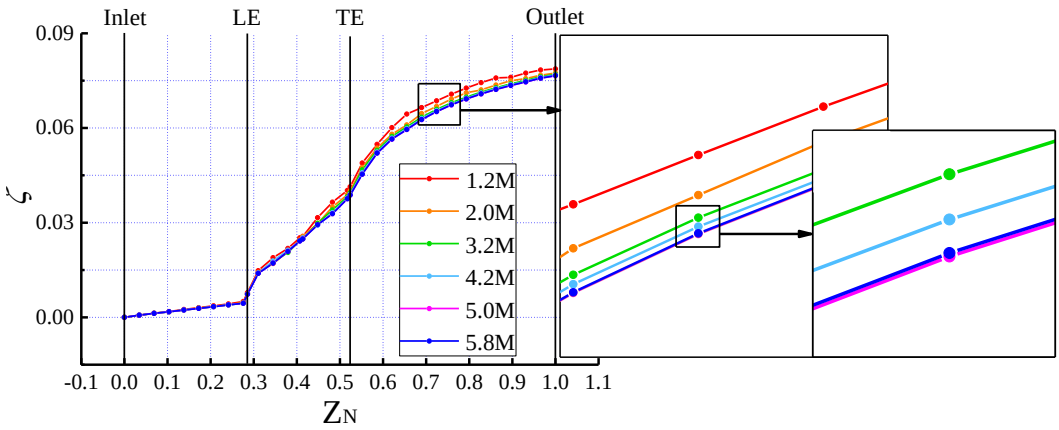


**Fig. 11. Variations of mass-flow average $\zeta$ along different axial cross-sections.**

end wall was effectively weakened, and the corner separation point was delayed by the application of a positive lean blade (Ding *et al.* 2018; Fischer *et al.* 2004). The development of the boundary layer near the end-wall was the main reason for producing the vortex structures and blocking the blade passage. Therefore, research about 3D blade formation has not been limited to discussing the design of stacking lines. In recent years, the local shape of the blade near the end-wall gradually has become a matter of concern for scholars (Lin *et al.* 2013; Wang *et al.* 2018).

The wavy blade-end was proven to be able to effectively reduce the total pressure loss and enhance the static pressure rise by Wang *et al.* (2018). However, the parameters of the blade profile have not been quantified. In this study, the shape of the blade-end was further optimized and discussed. Figure 12 introduces the schemes of the three kinds of wavy blade-ends. As shown in Fig. 12a, a one-period sinusoidal curve was applied in the scheme of the LE/TE (leading edge/trailing edge) near the end-wall. The wave moving toward the PS (pressure surface) was defined as a peak (red blade profile), and the wave moving toward the SS (suction surface) was a trough (blue blade profile). The wavelength was expressed in "H", and the amplitude was expressed in "A". Based on the design of LE/TE, we proposed the 3D geometric configurations of the cascade with the wavy blade-end as shown in Fig. 12b. Because of the profile of the cascade being designed based on the stator from the last stage of a high-load axial compressor, a uniform exit flow angle was important. To maintain the airflows out from the passage along the Z-axis direction, we proposed two kinds of wavy blade-ends with a straight trailing edge (WBE_R and WBE_S). The relevant descriptions are as follows:

1. WBE_P. The compound lean composed of a positive lean and a negative lean is applied in the baseline blade near the end-wall, and the corresponding vertical view is shown in Fig. 13. The red blade profile is the positive lean element, and the blue blade profile is the negative lean element. The direction of the movement of the elements is parallel to the chord line, so the cascade is named WBE_P (wavy blade-end_parallel).
2. WBE_R. The blade trailing edge is still a straight line. The positive lean element rotates counterclockwise, and the negative lean element rotates clockwise at the center of the TE. Therefore, the cascade is named WBE_R (wavy blade-end_rotate). Additionally, the LEs of the positive lean element and the negative lean element are adjusted to coincide with the peak and trough of the wavy curve, respectively.
3. WBE_S. The straight line is also used as the trailing edge, and the straight leading edge is replaced by the sinusoidal curve. In particular, the rear half (near the TE) of the positive lean element and the negative lean element still coincide with the baseline profile. Only the

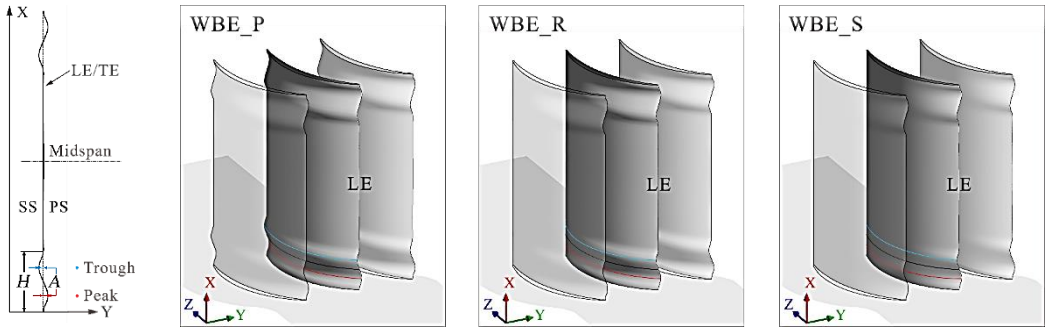


**a. Scheme of curve** **b. 3D geometric configurations**

**Fig. 12. Schemes of the three wavy blade-ends.**

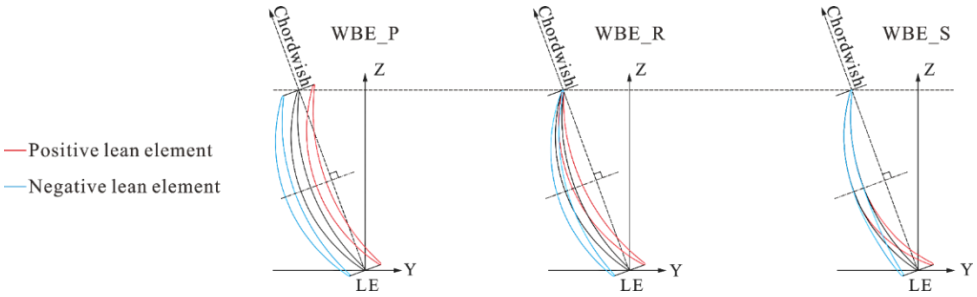


**Fig. 13. Vertical views of the blade profile.**

front half is adjusted to match the wavy curve. As seen in Fig. 12b, the scheme makes the blade surface smoother. Therefore, the cascade is named WBE_S (wavy blade-end_smooth).

## 5. NUMERICAL RESULTS

### 5.1 Flow performance of baseline cascade

For a 3D corner stall, as an unsteady flow affects the compressor performance, the flow phenomenon leads to a serious blockage of the blade passage near the end-wall and destroys the compressor stability. Scholars (Lei *et al*. 2008; Xianjun *et al.* 2010; Lieblein and Johnsen 1961) have developed a series of models to forecast the occurrence of a corner stall. The prediction model for corner separation/stall is used to guide compressor design. In this study, we carried out the experimental measurement of the baseline cascade only for the design condition, so the prediction model can be used to predict the stall condition of the cascade.

A prediction model of the corner stall considering the influence of the 3D geometric aerodynamic parameters on the corner separation was proposed by Xianjun *et al.* (2010). The evaluating indicator is defined as diffusion parameter $D_m$, and the formula is given as follows:

$$D_{\mathrm{m}}=\frac{\left(\cos\alpha_1+\cos\alpha_2\right)^2\sin\frac{\varphi}{2}}{\tau\cos^2\alpha_2}\left[1-\left(\frac{\cos\alpha_1}{\cos\alpha_2}\right)^2\right]AR^{0.18} \quad (2)$$

where the solidity $\tau$, aspect ratio AR, blade camber angle $\varphi$, inlet flow angle $\alpha_1$, and outlet flow angle $\alpha_2$ reflect the streamwise pressure gradient and the pitchwise pressure gradient. The model can effectively predict the corner stall of the 3D cascade. Based on the numerical results of more than 200 different cascades by Xianjun *et al.* (2010), we found that because the value of $D_m$ was larger than 0.47±0.015, the cascade could enter the corner stall. According to Xianjun *et al.* (2010), the critical range of the diffusion parameter is $D_{\mathrm{m,cr}}\geq0.47\pm0.015$ ($D_{\mathrm{m,cr}}\geq0.455$).

The values of the diffusion parameter $D_{\mathrm{m}}$ and the typical flow field characteristics of the baseline are shown in Fig. 14. The cases that may enter the corner stall are covered by blue slashes (the range is $0.455\geq D_{\mathrm{m}}\geq0.47$). When the incidence was bigger than 6°, the corresponding value of $D_{\mathrm{m}}$ was higher than 0.455. At the same time, the corner stall could occur. The low-energy fluids of the blade suction surface at typical incidences are shown in Fig. 14. The regions are represented by the 3D iso-surfaces of the axial velocity<0.001 and are covered in gray.

At the 6° incidence, although more low-energy fluids accumulate near the blade suction surface, the flow field was still stable and maintained the strict vertical symmetrical structure. When the incidence increased to 7°, the symmetrical low-energy fluids increased and interacted along the spanwise direction. The interaction between the two parts of the flow field (the upper part and lower part) led to the flow-field structure becoming an asymmetric structure, which

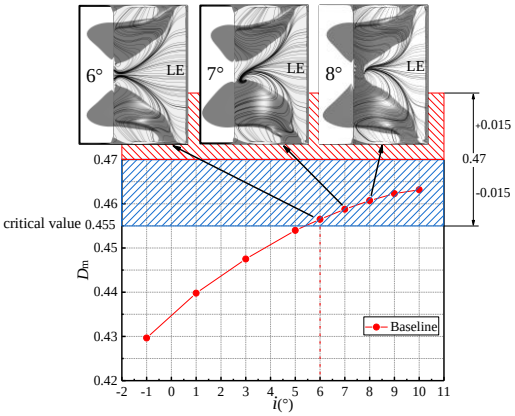


**Fig. 14. Diffusion parameter $D_{\mathrm{m}}$ and low-energy fluid at typical incidences.**

meant that the flow performance became an unsteady condition. With the incidence consistently increasing to 8°, more low-energy fluid accumulated near the lower end-wall, the corner separations continuously expanded along the spanwise and connected to each other. Additionally, the separation type was switched to an open separation (Shan Ma *et al.* 2019), and the corner stall was considered to have occurred.

The separations were formed by the accumulated low-energy fluid and complex vortex structures, which were the main reason for the flow loss. Therefore, we compared and discussed the flow fields of the cascade at the -1° and 7° incidences. Figure 15 shows the streamlines near the walls at the two conditions, and some special 3D vortices near the end-wall are given in the partially enlarged views. As shown in the figure, the end-wall is replaced by the contour of the pitchwise pressure gradient $|\partial P/\partial y|$, and the blade is colored by the contour of the radial pressure gradient $|\partial P/\partial x|$. The low-energy fluid is shown by the iso-surface, and the color is gray.

1. Low-energy fluid around the LE

The formation of a horseshoe vortex resulted in the accumulation of low-energy fluid around the leading edge near the end-wall. At the -1° incidence, the generation of the horseshoe vortex was closely related to the node $N_1$ and Saddle $S_1$. As shown in the partially enlarged view ①, because of the obstruction of the blade, the higher speed airflow (red streamlines) flowed to the end-wall and produced the node N1. The lower speed airflow (blue streamlines) met the higher speed airflow and formed the saddle point S1. The airflow from the saddle point S1 was divided into two legs. The part entering the blade passage near the suction surface rolled up and then formed the suction surface leg of the horseshoe vortex. The other part entered the blade passage near the pressure surface, which was named the pressure side leg of the horseshoe vortex.

As the incidence increased to 7°, an asymmetric flow field emerged. As shown in the partially enlarged view ①, the formation mechanism of the horseshoe vortex was the same as the design condition. However, the increase of the incidence changed the

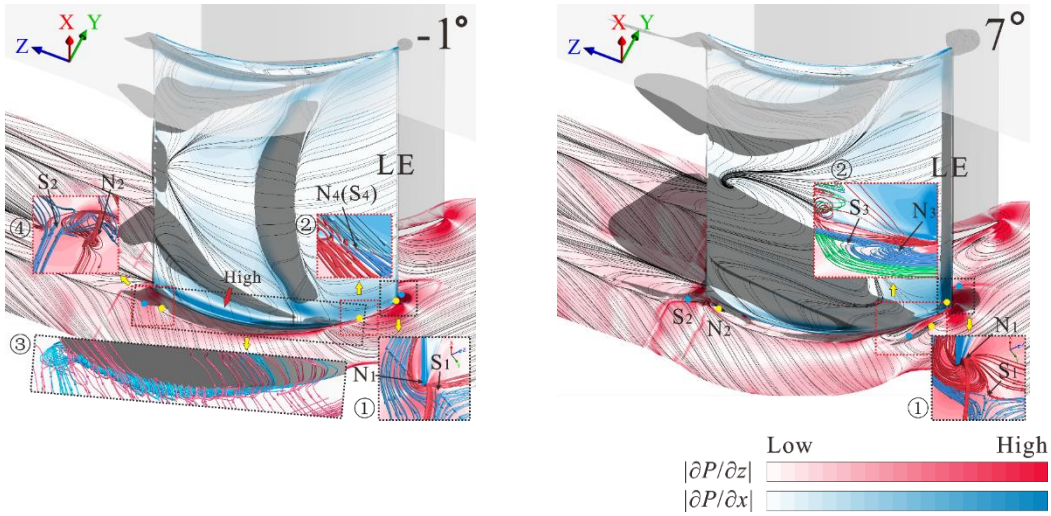


**Fig. 15. Flow characteristics cascade passage at -1° and 7° incidences.**

incoming flow direction, which led to the suction side leg of the horseshoe vortex requiring a bigger deflection angle to enter the cascade passage. Therefore, more low-energy fluid was accumulated on the end-wall near the leading edge.

2. Corner separation

On the left side of Fig. 15, the partially enlarged view ② shows the initial position of the corner separation. After the suction, the side leg of the horseshoe vortex entered the blade passage, which reattached to the blade suction surface at a fast speed with the pitchwise pressure gradient. Subsequently, the leg met the corner vortex and formed a multicritical point $N_4(S_4)$. The point had a dual meaning. $N_4$ was a reattachment point of the horseshoe vortex, and $S_4$ represented an initial location of the separation line on the blade suction surface. Some of the low-energy fluid accumulated near the blade suction surface under the axial reverse pressure. Therefore, $N_4(S_4)$ was considered to be the initial point of the 3D corner separation, and the same could be found at 7° incidence. The development of the corner vortex affected the axial range of the corner separation.

3. Corner vortex

As shown in the partially enlarged view ④ of Fig. 15, part of the boundary layer (blue streamlines) met the low-energy fluid from the blade pressure surface (red streamline), and a saddle point $S_2$ was formed. Part of the airflow (blue streamlines) moved upstream along the corner range, and the corner vortex (blue streamlines in the partially enlarged view ③) was formed with the influence of the passage vortex.

The generation of the main vortex structures was closely related to the development of the boundary layers. The appearance of vortices was always accompanied by flow loss. Therefore, a method of changing the distribution of the boundary layer could be developed to suppress the accumulation of low-energy fluid and to reduce the flow loss.

## 5.2 Effects of wavy blade-end on the cascade performance

The development of the boundary layer near the end-wall affects the accumulation of the low-energy fluid and the generation of the flow loss. Therefore, the wavy blade was applied only in the cascade near the end-wall and was named the wavy blade-end. In this study, we selected the wavelength "*H*" and amplitude "*A*" to discuss the effect of the geometric parameters on the cascade performance. To quantitatively analyze the parameters, the ratio of *A/H* was defined.

The values of the amplitude can be written as a column matrix with a size of 5×1: $A = [0.02t,0.03t,0.04t,0.05t,0.06t]^{-1}$. The values of the wavelength form a column matrix with a size of 4×1: $H = [0.15h,0.2h,0.25h,0.3h]^{-1}$. Therefore, a matrix with a size of 5×4 formed by $A/H = AH^{-1}$ is obtained, as follows:

$$A/H = D\times\frac{t}{h} = \begin{bmatrix} \frac{2}{15} & \frac{2}{20} & \frac{2}{25} & \frac{2}{30} \\ \frac{3}{15} & \frac{3}{20} & \frac{3}{25} & \frac{3}{30} \\ \frac{4}{15} & \frac{4}{20} & \frac{4}{25} & \frac{4}{30} \\ \frac{5}{15} & \frac{5}{20} & \frac{5}{25} & \frac{5}{30} \\ \frac{6}{15} & \frac{6}{20} & \frac{6}{25} & \frac{6}{30} \end{bmatrix} \times \frac{t}{h} \quad (3)$$

The common divisor *t*/*h* was extracted, and the remaining matrix was represented by *D* (Database). The *A/H* with the 20 values was defined to quantitatively discuss the influence of the amplitude and the wavelength on the compressor cascade. The optimized object was only WBE_P, and the optimized parameters were applied for WBE_R and WBE_S for further comparison and discussion.

1. Performance of cascade with WBE_P

The wavy blade-end of WBE_P in Fig. 12b is discussed first. According to the analysis in Section

5.1, the flow field of the baseline at 6° incidence was still stable, so we selected this condition for further comparison and discussion. The total pressure loss coefficient $\zeta$ of the cascade with WBE_P is shown in Fig. 16. To facilitate analysis, we classified WBE_P with the same wavelength into one group for discussion. Therefore, four series of data could be obtained, and the wavelengths were 0.15 *h*, 0.2 *h*, 0.25 *h*, and 0.3 *h*. The $\zeta$ of the baseline is represented by the red line, and the value is 0.1021. The minimum total pressure loss coefficients of the four series of data are highlighted by the green circles. When the wavelengths were 0.2*h* and 0.25*h*, the lowest value of $\zeta$ could not be obtained based only on the data from Formula (3). Therefore, we calculated the additional cases with $A$ = 0.07 $t$ and 0.8 $t$. The corresponding values of $\zeta$ are highlighted by the blue circles.

As shown in Fig. 16, the $\zeta$ followed a trend of first decreasing and then increasing with the rise of the wavelength "*H*" from 0.15 *h* to 0.3 *h*. Significantly, once the wavelength increased to 0.3 *h*, the $\zeta$ was still higher than the baseline, regardless of the value of the amplitude. Therefore, the wavy blade-end with a longer wavelength was detrimental to the cascade performance. Furthermore, for the other three groups with the wavelength range of 0.15–0.25 *h*, the range of *D* with the lowest total pressure loss was 0.28–0.33.

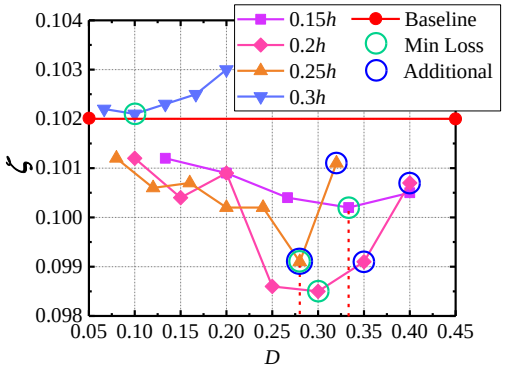


**Fig. 16. Effect of WBE_P on total pressure loss at 6° incidence.**

Furthermore, the optimum case could be obtained when the wavelength was 0.2 *h* and the value of the *D* was 0.3. The corresponding total pressure loss coefficient was 0.0985. The value decreased by 5.49% compared with the baseline. Therefore, we selected the optimum case for the further flow-field analysis to discuss the function of the wavy blade-end, and the $H$ = 0.2 *h*, $A$ = 0.06 *t*.

The relationships of the WBE_P' geometric parameters and the cascade performances at 6° incidence are shown in Fig. 17. The values of $\zeta$ are colored by the contours. To quantify the effects of the wavelength and the amplitude on the cascade performance, the transverse axis is represented by *A/t*, and the longitudinal axis is represented by *H/h*. The contour is represented by nine contour lines. The

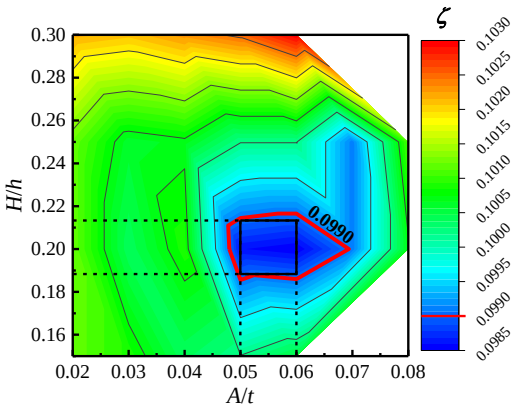


**Fig. 17. Effects of the wavelength and amplitude on the $\zeta$.**

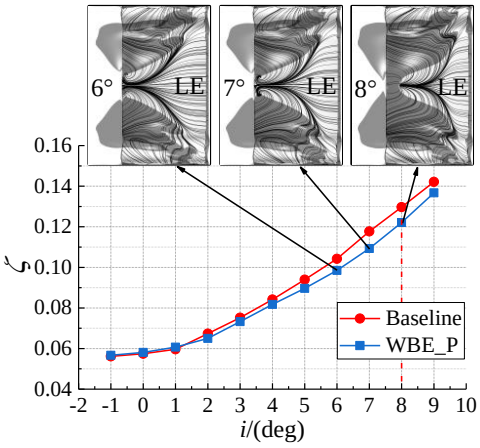


**Fig. 18. Variations of $\zeta$ with different incidences.**

$\zeta$ inside the range surrounded by the first contour line (red line) was smaller than 0.099. If the value of *A/t* was between 0.05 and 0.06 and the *H/h* was in the range of 0.188 to 0.214 at the same time (black rectangle), the smaller $\zeta$ could be obtained.

As displayed in Fig. 18, the comparisons of $\zeta$ between the baseline and WBE_P could be found. As the incidence increased to be larger than 1°, the $\zeta$ followed an obvious decreasing trend because of the application of WBE_P. At the 6° and 7° incidences, as shown in the range of accumulated low-energy fluids, the flow fields were always vertically symmetrical. When the incidence increased to 8°, the 3D corner separation became an open separation, and the stall flow field occurred. Above all, the total pressure loss was reduced by WBE_P under almost all conditions ($i$>1°). However, no significant advantages were achieved by delaying the occurrence of a corner stall.

Figure 19 shows the effects of WBE_P on the cascade performance at 6° incidence. The low-energy fluid is covered by the gray iso-surfaces of the axial velocity<0.001, and the distributions of $\zeta$ are extracted from the trailing edge. The radial pressure gradient $|\partial P/\partial x|$ on the blade suction surface is shown to compare the change of the blade load, and the

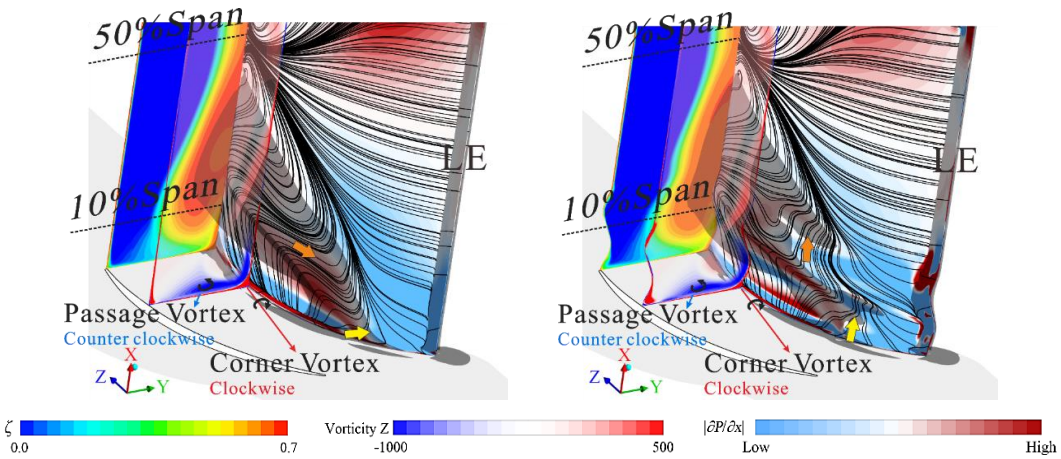


**Fig. 19. Comparison of flow field details at 6° incidence. Left: Baseline; Right: WBE_P.**

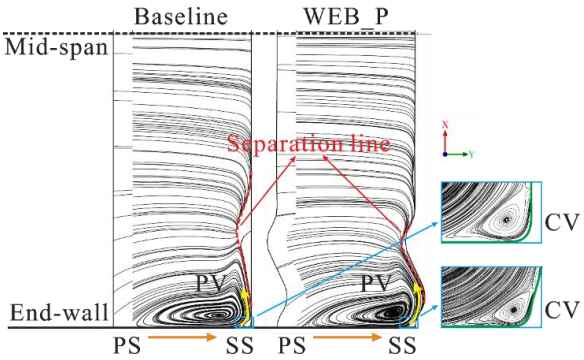


**Fig. 20. Two-dimensional limiting streamlines at the planes of 50%*Ca*.**

contours from the component in the z-axis direction of vorticity Z are shown at the cross-sections of 70%*Ca*.

As shown in Fig. 19, the intensities of the passage vortex and corner vortex were weakened by the application of the wavy blade-end because the boundary layer and the static pressure near the walls were redistributed. For the range near the blade suction surface, the negative lean element moved toward the blade suction surface and formed a concave profile, and a high-static pressure area appeared near the end-wall. This led to part of the low-energy fluid moving away from the range near the LE, and the corresponding limiting streamlines showed an obvious climbing trend. The directions were represented by the yellow arrow. Another concave profile also could be found in the upper range of the positive lean element. The low-energy fluid also was removed and the flow reversal streamlines became a climbing trend (orange arrow).

As shown in Fig. 20, to further analyze the flow field, we obtained the two-dimensional limiting streamlines at the planes of 50%*Ca*. In the baseline, the end-wall boundary layer moved away from the PS to SS under the influence of the pitchwise pressure gradient, and the passage vortex (PV) was formed. When the boundary layer encountered the straight blade, there was a large angle turning in the flow direction. This contributed to a large separation range appearing near the blade suction surface. As the wavy blade-end was used in the cascade, the included angle between the end-wall and suction surface was enlarged by the concave profile near the end-wall. More released space was provided for the passage vortex, which led to a smoother turning angle when the airflow climbed upward along the spanwise, and the range of the corner vortex was reduced. As the boundary layer moved upward along the blade suction surface, the airflow was always attached to the blade suction surface, and the significant separation disappeared.

The $\zeta$ decreased significantly by the application of the wavy blade-end along the spanwise direction. Figure 21 shows the mass-flow averaged $\zeta$ along the spanwise direction at the axial cross-section of the trailing edge to compare the advantage of WBE_P. The $\zeta$ inside the range of the 10–90% span with the wavy blade-end was applied, and only the $\zeta$ near the end-wall (0–10% span, 90–100% span) was enhanced. The blocked range of the blade passage is colored in gray and shown on the right of Fig. 21. We determined the borders by referring to Khalid (1995). The blocked range is formed by a term ($\rho v_m$), and the formula $|(\rho v_m)|_{x,\ y}$ can be used to calculate the blockage of the axial cross-section. The criterion of the edge of the blocked range is provided as follows:

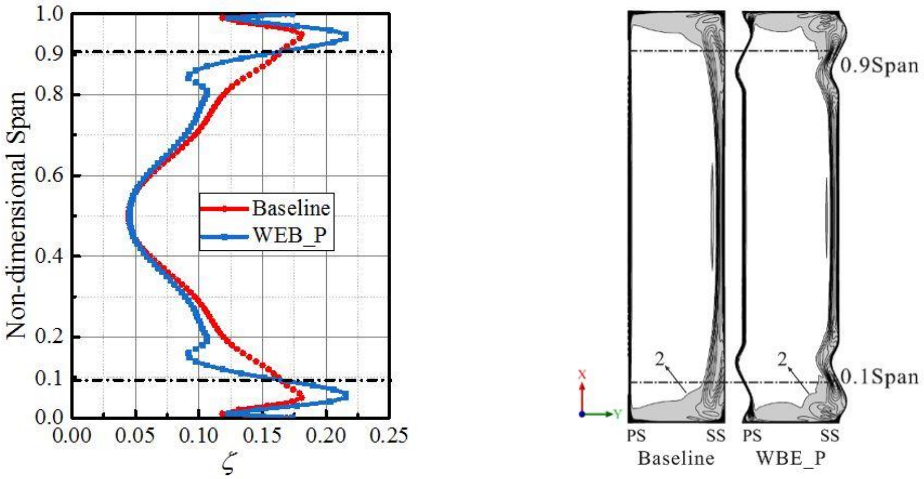


**Fig. 21. Cascade performance along the spanwise direction. Left: mass-flow averaged ζ; Right: blocked ranges.**

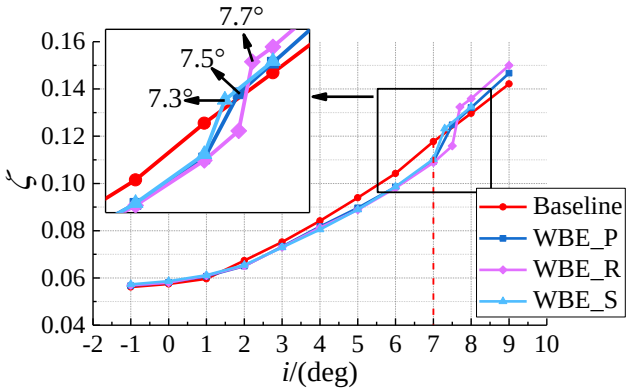


**Fig. 22. Variations of ζ with increasing incidences.**

$$\left|\nabla\left(\rho v_{\mathrm{m}}\right)\right|_{x,y} \Big/ \left(\rho_{\mathrm{in}} v_{\mathrm{in,m}} / C\right) = 2 \tag{4}$$

where $\rho$ is the local density, the variable $v_m$ is the velocity component of the local main flow, $\rho_{in}$ is the density of the inlet, and $v_{\mathrm{in,\ m}}$ is the velocity component of the main flow at the inlet. As shown on the right side of Fig. 21, the blocked range is decreased by the application of WBE_P.

2. Comparison of the three wavy blade-ends

The $\zeta$ of the three kinds of wavy blade-end at different incidences are shown in Fig. 22. As the three wavy blade-ends were applied in the cascade, the $\zeta$ could be reduced effectively by WBE_P, WBE_R, and WBE_S when the incidence was bigger than 1°. As the incidence increased to 7°, the stall still had not happened for the three cascades with WBE. For further comparison, we calculated more cases. The corner stall of WBE_P occurred at the 7.5° incidence, which was delayed to a 7.7° incidence by WBE_R.

When the incidence was in the range near the design condition (incidence < 2°), the total pressure loss was enhanced by the use of these wavy blades. For WBE_R, the total pressure loss increased only by 1% at -1° incidence, whereas the $\zeta$ was reduced by 7.6% at 7° incidence, and the occurrence of the stall was delayed. Therefore, the sacrifice of the 1% design condition performance could be considered to improve the performance at the large incidence and delay the occurrence of the stall.

To compare the performance of the three wavy blade-ends more comprehensively, more aerodynamic parameters of the baseline and the cascade with wavy blade-ends at 6° incidence are listed in Table 2. We selected the static pressure coefficient *Cp* to evaluate the capability to enhance the static pressure, and the coefficient is expressed as follows:

$$Cp(x,y,z) = \frac{Pt(x,y,z) - Pt_{in}}{Pt_{in} - P_{in}} \tag{5}$$

We calculated the dimensionless value of $A_b/A_{in}$ to evaluate the extent of blockage in the blade passage. $A_b$ represents the area of the blocked range at the measurement plane, and $A_{in}$ is the area of the inlet boundary. In Table 2, the optimum performance values are shown in bold. The variations of the aerodynamic parameters are shown in Fig. 23. We

**Table 2. Effects of wavy blade-end on the aerodynamic performance at 6° incidence**

| Cases | $\zeta$ | $Cp$ | $A_b/A_{in}$ |
|---|---|---|---|
| Baseline | 0.10419 | 0.4467 | 0.0841 |
| WBE_P | 0.09847 | **0.4648** | 0.0734 |
| WBE_R | **0.09811** | 0.4612 | **0.0725** |
| WBE_S | 0.09863 | 0.4614 | 0.0760 |

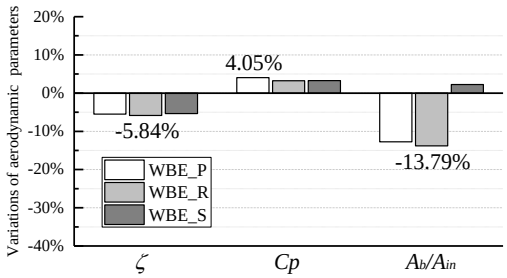


**Fig. 23. Variations of main parameters of cascade with WBEs.**

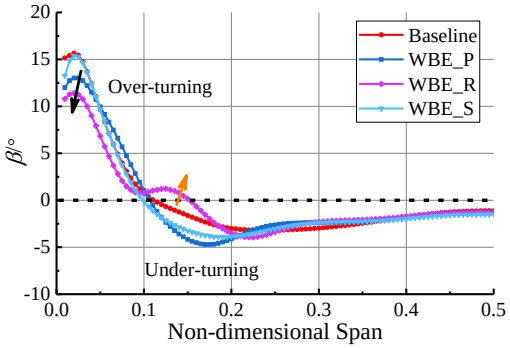


**Fig. 24. Pitchwise-averaged flow angle along the spanwise at the 0.4*Ca* downstream of the TE (6° incidence).**

obtained the minimum $\zeta$ and the blocked blade passage with the application of WBE_R, and the reductions reached 5.84% and 13.79%. The highest *Cp* was obtained with WBE_P, and the degree of increase was 4.05%. Moreover, even if the aerodynamic performance of the baseline was improved by the utilization of WBE_S, the capacity was weakest in the three wavy blade-ends, and WBE_R showed an obvious advantage.

The distributions of the pitchwise-averaged flow angle along the half-spanwise direction at 0.4*Ca* downstream of the TE are given in Fig. 24. The overturning of the flow angle represented the existence of a larger flow turning angle in the range, and higher blade loads could be obtained. However, the underturning of the flow angle meant that more low-energy fluid accumulated in the corresponding range. To a certain extent, the blade loads near the end-wall were weakened with the application of WBE_R and WBE_S because the flow angle was reduced in the overturning range. In the underturning range, the flow angle inside the 10–20% span was increased by WBE_R, which meant that the low-energy fluid was removed in this range. Therefore, the application of WBE_R was beneficial for the airflow flowing out the blade passage along the Z-axial direction.

The mass-flow averaged $\zeta$ along the spanwise direction and the contours of $\zeta$ at the axial cross-section of the trailing edge are shown in Fig. 25. In the left view, the total pressure loss was reduced effectively along the full span by the WBE_R compared with the baseline. This also was found in the contour. The flow-field characteristics of the cascade were improved by the applications of WBE_P and WBE_R. Especially near the midspan, WBE_R showed an advantage in the reduction of the $\zeta$. Considering the difference in the structure for

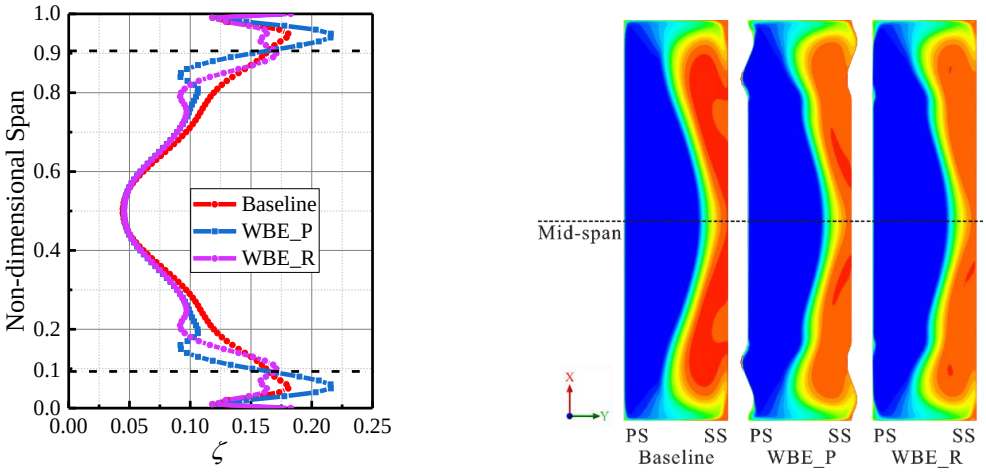


**Fig. 25. Cascade performance along the spanwise direction. Left: mass-flow averaged $\zeta$; Right: cloud images of $\zeta$**

WBE_P and WBE_R, the reduction of the $\zeta$ was mainly the result of the wavy blade near the leading edge. Moreover, the exit airflow angle along the Z-axial direction was beneficial because the cascade was designed based on a stator from the last stage of a high-load axial compressor. Therefore, WBE_R with a straight trailing edge was more suitable for use in improving the stator of the last stage to improve the compressor performance.

## 6. CONCLUSION

The compound lean modeling technique can redistribute the boundary layer near the walls to improve the performance of a compressor. Referencing the same design procedures of our predecessors, we quantitatively analyzed and discussed the parameters affecting the wavy blade-end, the wavelength, and the amplitude. In addition, we obtained an optimized conclusion to guide the design and optimization principles. Furthermore, we proposed two kinds of new wavy blade-ends and discussed each separately. The following conclusions can be drawn:

1. The wavelength and the amplitude of the wavy blade-end were further discussed as the main geometric parameters. To quantitatively analyze the parameters, the ratio of the wavelength divided by amplitude (*A/H*) was defined. When the wavelength "*H*" increased to 0.3 times the blade height, the $\zeta$ increased regardless of the value of the amplitude. The optimum case was obtained when the wavelength was 0.2 times the blade height h, the amplitude was 0.06 times the pitch *t* (*H/A* = 3.33 *h/t*), and the $\zeta$ and the area of the blocked range decreased by 5.49% and 12.72% compared with the baseline. Moreover, if the value of *A* was between 0.05 and 0.06 *t* and the *H* was between 0.188 and 0.214 *h* at the same time, a smaller flow loss could be obtained.
2. The wavy blade-ends with three geometric structures were proposed to discuss the influences. The wavy blade-end applied to the leading edge played a prominent role and was the main reason for the reduction of the $\zeta$. Comparing the performances of WBE_P (wavy trailing edge) and WBE_R (straight trailing edge), if the wavy blade-end was adopted in the LE and the TE was straight (WBE_R), the flow-field characteristics were further improved at large incidence. The $\zeta$ and the area of the blocked range decreased by 5.84% and 13.79% compared with the baseline. Moreover, WBE_R with a straight trailing edge showed an advantage in extending the stable operating range compared with WBE_P, and the corner stall point was delayed from 7.5° to 7.7°.
3. Because the profile of the cascade was designed based on the stator from the last stage of a high-load axial compressor, a uniform exit flow angle was important, and the exit airflow angle along the Z-axial direction was beneficial. Therefore, the two kinds of wavy blade-ends with straight trailing edges were compared. WBE_S with a smoother blade surface did not show an advantage in decreasing the $\zeta$ or the area of the blocked range. The cascade performance was improved by WBE_R, and the direction of the exit flow angle was closer to the Z-axis direction. Therefore, the WBE_R was more suitable for use in improving the stator of the last stage to improve the compressor performance.

Following are the main suggestions for future wavy-blade research: First, the wave near the blade-end should be lower than 0.3 times the blade height. Second, the wavy leading edge is necessary, and the wavy trailing edge is not necessary. Third, if the wavy blade-end is further studied, the conclusions of this research should be applied in a real compressor environment to determine the feasibility of a wavy blade-end.

## ACKNOWLEDGEMENTS

This study was co-supported by the financial support of the Civil Aviation Flight University of China Scientific research fund (J2021-012, ZJ2021-08, J2019-019), National Natural Science Foundation of China (U2133209).

## REFERENCES

Bearman, P. W. and J. C. Owen (1998). Reduction of Bluff-Body Drag and Suppression of Vortex Shedding by the Introduction of Wavy Separation Lines. *Journal of Fluids & Structures* 12(1), 123-130.

Benini, E. and R. Biollo (2007). Aerodynamics of swept and leaned transonic compressor rotors. *Applied Energy* 84(10),1012-1027.

Denton, J. D. (1993). Loss mechanisms in turbomachines. *Journal of Turbomachinery*, 115, 621-656.

Ding J, S. Wang, X. Hao, L. Cai, Z. Wang and J. Shen (2018). The effect of aspiration configuration on aerodynamic performance in compound lean compressor cascades of gas turbines. *Applied Thermal Engineering* 130, 264–278.

Fischer, A., W. Riess and J. R. Seume (2004). Performance of Strongly Bowed Stators in a 4-Stage High Speed Compressor. *Journal of Turbomachinery* 126 (3), 333.

Hartland, J. C., D. G. Gregory-Smith, N. W. Harvey, and M. G. Rose (2000). Nonaxisymmetric turbine end wall design: Part II—Experimental validation. *Journal of Turbomachinery* 122(2), 286–293.

Hergt, A. and U. Siller (2015). About Transonic Compressor Tandem Design a Principle Study. *Proceeding of ASME Turbo Expo*, Montréal, Canada.

Jiabin, L., L. Ji and W. Yi. (2018).The Use of Blended Blade and End Wall in Compressor Cascade: Optimization Design and Flow Mechanism. *Proceeding of ASME Turbo Expo*, Oslo, Norway.

Khalid, S. A. (1995). The effects of tip clearance on axial compressor pressure rise, *Massach Inst Tech*.

Kiran, K. N. and S. Anish (2017). An investigation on the effect of pitchwise endwall design in a turbine cascade at different incidence angles. *Aerospace of Science and Technology* 71,382–391.

Lei, V. M, Z. S. Spakovszky and E. M. Greitzer (2008). A Criterion for Axial Compressor Hub-Corner Stall. *Journal of Turbomachinery* 130, 031006.

Li, X., W. Chu and Y. Wu (2014). Numerical investigation of inlet boundary layer skew in axial-flow compressor cascade and the corresponding non-axisymmetric end wall profiling. *Proceedings of the Institution of Mechanical Engineers Part A: Journal of Power & Energy* 228 (6), 638-656.

Li, Z. and Y. Liu (2017). Blade-end Treatment for Axial Compressors Based on Optimization Method. *Energy* 126, 217-230.

Lieblein, S. and I. A. Johnsen (1961). Resume of Transonic-Compressor Research at NACA Lewis Laboratory. *Journal for Engineering for Power* 83(3), 219-232.

Lin, Y. F., K. Lam, L. Zou and Y. Liu (2013). Numerical study of flows past airfoils with wavy surfaces. *Journal of Fluids and Structures* 36,136-148.

Ma, S., W. Chu, H. Zhang, X. Li and H. Kuang (2019). A combined application of micro-vortex generator and boundary layer suction in a high-load compressor cascade. Chinese Journal of Aeronautics 32(5), 1171–1183.

Payyappalli, M. M. and A. M. Pradeep(2018). Effect of Tandem Blading in Contra-Rotating Axial Flow Fans. *Proceeding of ASME Turbo Expo*, Oslo, Norway.

Pope, A. J., S. C. Morris and A. Jemcov (2021). Performance of a Subsonic Compressor Airfoil with Upstream, End-wall Injection Flow. *Proceeding of ASME Turbo Expo*, Virtual, Online.

Subhra, S. K., S. Ayush, C. Huang and K. Joseph (2021). Effect of the Axial Casing Groove Geometry on the Production and Distribution of Reynolds Stresses in the Tip Region of an Axial Compressor Rotor. *Proceeding of ASME Turbo Expo*, Virtual, Online.

Sun, S., S. Wang and S. Chen (2020). The influence of diversified forward sweep heights on operating range and performance of an ultra-high-load low-reaction transonic compressor rotor. *Energy* 194 , 116857.

Sun, X., S. Ma, Z. Wang, J. Shi and L. Zhou (2021). Compressible flow characteristics in bent duct with constant flow section. *Proceedings of the Institution of Mechanical Engineers Part G: Journal of Aerospace Engineering*, 235 (7), 745-757.

Wang, B., Y. Wu and K. Liu (2018). Numerical Investigation of Passive Flow Control Using Wavy Blades in a Highly-Loaded Compressor Cascade. *Proceeding of ASME Turbo Expo*, Oslo, Norway.

Wellborn, S. R. and R. A. Delaney(2001). Redesign of a 12- Stage Axial- Flow Compressor Using Multistage CFD. *Proceeding of ASME Turbo Expo*, New Orleans, Louisiana.

Yu, X. and B. Liu (2010). A prediction model for corner separation/stall in axial compressors. *Proceeding of ASME Turbo Expo*, Glasgow, UK.

Zhang, Y. F.(2010). Investigations of end wall flow behavior and its control strategies in highly-loaded compressor [dissertation]. Xi'an: Northwestern Polytechnical University. [Chinese].